

Extended Cyclotron Resonant Heating of the Turbulent Solar Wind

TREVOR A. BOWEN,¹ IVAN VASKO,² STUART D. BALE,^{1,3} BENJAMIN D. G. CHANDRAN,⁴ ALEXANDROS CHASAPIS,⁵
THIERRY DUDOK DE WIT,^{6,7} ALFRED MALLET,¹ MICHAEL MCMANUS,¹ ROMAIN MEYRAND,⁸ MARC PULUPA,¹ AND
JONATHAN SQUIRE⁸

¹*Space Sciences Laboratory, University of California, Berkeley, CA 94720-7450, USA*

²*William B. Hanson Center for Space Sciences, University of Texas at Dallas, Richardson, TX, USA*

³*Physics Department, University of California, Berkeley, CA 94720-7300, USA*

⁴*Department of Physics & Astronomy, University of New Hampshire, Durham, NH 03824, USA*

⁵*Laboratory for Atmospheric and Space Physics, University of Colorado, Boulder, 80303, CO, USA*

⁶*LPC2E, CNRS and University of Orléans, Orléans, France*

⁷*ISSI, Bern, Switzerland*

⁸*Department of Physics, University of Otago, 730 Cumberland St., Dunedin 9016, New Zealand*

ABSTRACT

Circularly polarized, nearly parallel propagating waves are prevalent in the solar wind at ion-kinetic scales. At these scales, the spectrum of turbulent fluctuations in the solar wind steepens, often called the transition-range, before flattening at sub-ion scales. Circularly polarized waves have been proposed as a mechanism to couple electromagnetic fluctuations to ion gyromotion, enabling ion-scale dissipation that results in observed ion-scale steepening. Here, we study Parker Solar Probe observations of an extended stream of fast solar wind ranging from $\sim 15R_{\odot} - 55R_{\odot}$. We demonstrate that, throughout the stream, transition-range steepening at ion-scales is associated with the presence of significant left-handed ion-kinetic scale waves, which are thought to be ion-cyclotron waves. We implement quasilinear theory to compute the rate at which ions are heated via cyclotron resonance with the observed circularly polarized waves given the empirically measured proton velocity distribution functions. We apply the Von Kármán decay law to estimate the turbulent decay of the large-scale fluctuations, which is equal to the turbulent energy cascade rate. We find that the ion-cyclotron heating rates are correlated with, and amount to a significant fraction of, the turbulent energy cascade rate, implying that cyclotron heating is an important dissipation mechanism in the solar wind.

1. INTRODUCTION

Weakly collisional plasmas, which are common in astrophysical environments, are fundamentally governed by kinetic processes (Marsch 2006). Our understanding of kinetic processes responsible for turbulent dissipation, heating, and energy transfer in collisionless environments is relatively incomplete, and necessary to explain phenomena such as solar wind acceleration and coronal heating (Parker 1958; Richardson et al. 1995; Hellinger et al. 2013; Fox et al. 2016), and analogous astrophysical processes.

Recent work on the near-Sun solar wind has highlighted the significant presence of circularly polarized ion-scale waves (Bale et al. 2019; Bowen et al. 2020a), and their association with non-thermal features in particle distributions (Verniero et al. 2020; Klein et al. 2021;

Verniero et al. 2022). These waves are characterized by their quasi-parallel propagation along the magnetic field (Jian et al. 2014; Boardson et al. 2015; Bowen et al. 2020a; Liu et al. 2023). Electric field measurements suggest that these wave predominantly propagate outward from the sun (Bowen et al. 2020b), similar to the observed propagation direction of larger-scale Alfvénic turbulent fluctuations (Roberts et al. 1987; Tu & Marsch 1995; Bavassano et al. 1998; McManus et al. 2020).

While ion-scale waves are often associated with processes related to kinetic plasma distributions, e.g. instabilities and resonant damping, (Gary 1993; Isenberg & Lee 1996; Hollweg & Markovskii 2002; Marsch 2006; Klein et al. 2018, 2021), they may also serve as a mechanism to transfer turbulent energy via cyclotron resonance to particle thermal motion (Hollweg & Johnson 1988; Tu & Marsch 1997; Cranmer 2000; Hollweg & Isenberg 2002; Cranmer 2014). Signatures of quasilinear cyclotron resonance in the observed proton distribution

functions have been suggested in various spacecraft observations (Marsch & Tu 2001a; He et al. 2015; Verniero et al. 2022; Bowen et al. 2022). Furthermore, steepening of turbulent spectra at ion cyclotron resonant scales has been interpreted as a signature of cyclotron resonant damping (Denskat et al. 1983; Woodham et al. 2018; Lotz et al. 2023) and is correlated with the presence of circularly polarized signatures (Goldstein et al. 1994; Leamon et al. 1998; He et al. 2011; Lion et al. 2016; Zhao et al. 2021). These helical signatures are both correlated with proton temperature anisotropy as well as the turbulent amplitudes (Telloni et al. 2019), suggesting they may be associated with turbulent dissipation.

The quasilinear damping of the *in situ* population of ion cyclotron waves (ICW) has been measured with a heating rate accounting for 10-20% of the turbulent energy flux (Bowen et al. 2022). Further studies have shown the direct transfer of energy from waves to protons using wave-particle correlation methods (Vech et al. 2020; Luo et al. 2022). The presence of these waves has been observed to correlate both to turbulent features such as the large-scale cross helicity and sub-ion-scale intermittency (Bowen et al. 2023).

In this Letter, we study an extended stream of fast solar wind observed by PSP from ~ 15 to $55R_{\odot}$ with persistent signatures of left-hand polarized waves. We show that left-handed polarization directly corresponds to turbulent steepening in the ion-kinetic scale transition range (Sahraoui et al. 2009; Kiyani et al. 2009; Bowen et al. 2020c; Duan et al. 2020, 2021), which has historically been interpreted as a signature of dissipation (Denskat et al. 1983; Goldstein et al. 1994; Leamon et al. 1998; Smith et al. 2006, 2012; Lion et al. 2016; Bowen et al. 2020c, 2023). Using the cold plasma dispersion to determine the internal energy and Poynting flux of the measured wave spectrum suggests that the energy to generate waves is stored within the turbulent fluctuations, indicating that the waves are a pathway to ion-scale turbulent dissipation. By applying drifting bi-Maxwellian fits to the distribution function, we estimate the empirical quasilinear heating rate of the local ion-scale waves (Kennel & Engelmann 1966; Isenberg & Lee 1996; Bowen et al. 2022). We similarly estimate local turbulent dissipation rates via turbulent amplitudes and the Von Kármán decay law to determine the decay of the largest, outer-scale turbulent fluctuations (Hosain et al. 1995; Wan et al. 2012; Bandyopadhyay et al. 2020; Wu et al. 2022). We demonstrate strong correlations between the quasilinear heating and turbulent dissipation rates. These strong correlations are evident in both global scaling as well as local fluctuations in the turbulent cascade and quasilinear heating rates. These

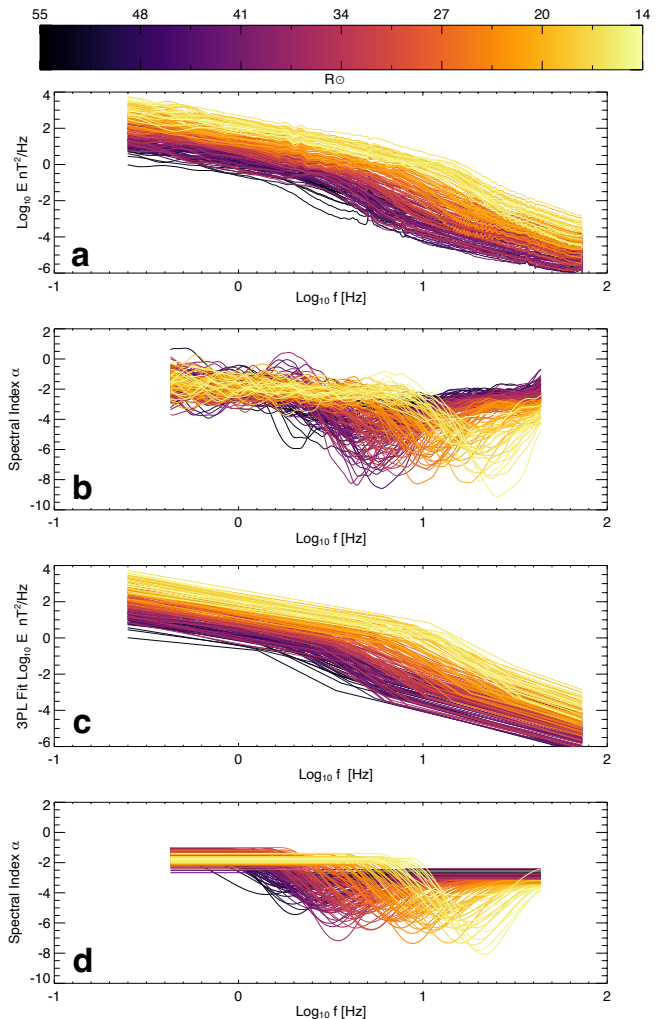


Figure 1. a) Measured spectral densities from Nov 16-20, 2021 computed for 6737 intervals of 128 s. Every 40th spectra is plotted. Colors represent radial distance of PSP from the sun, ranging from $\sim 14 - 55 R_{\odot}$, with light colors representing small distances becoming darker to indicate increasing distance. b) Local spectral index α of measured spectral densities computed in moving window. c) Three power-law fit (3PL) to observed spectra for each interval. d) Local spectral index α of 3PL spectral densities computed in moving window.

results suggest that cyclotron heating plays an important role in extended solar wind heating. These results may have strong implications for the nature of ion-scale heating in the corona and other weakly-collisional astrophysical plasmas.

2. METHODS & RESULTS

We focus on a stream of fast solar wind observed in the inner heliosphere by Parker Solar Probe (PSP) from 11/16/2021 to 11/20/2021. During this interval PSP was flying inwards towards the sun in near co-rotation

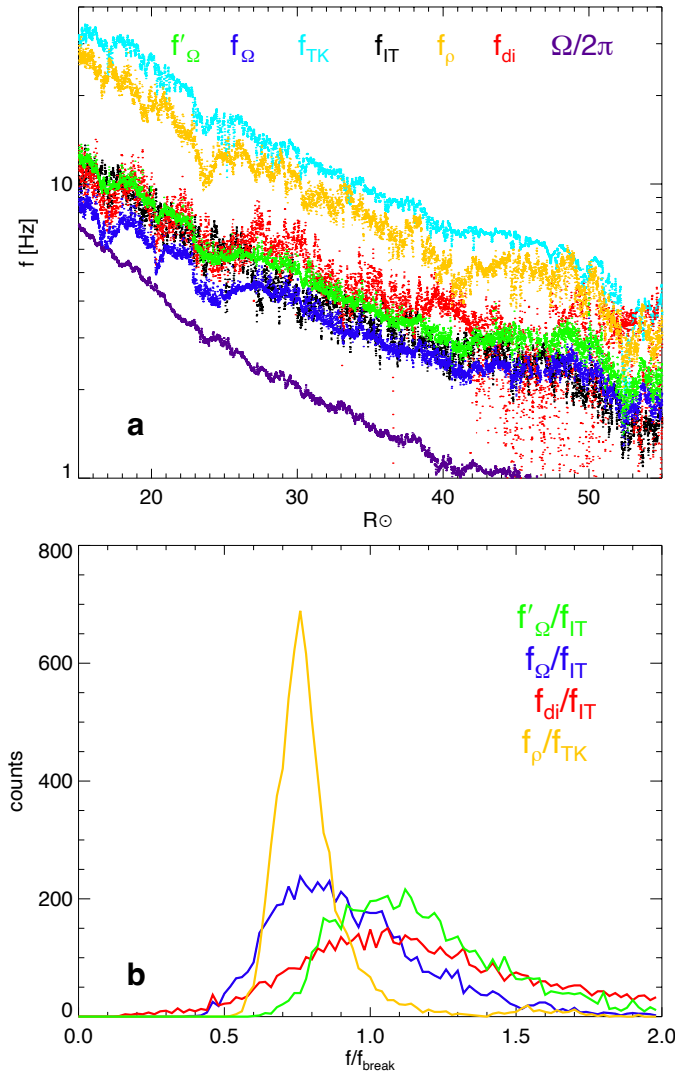


Figure 2. a) Frequencies corresponding to ion-kinetic scales computed with the Taylor Hypothesis for 6737 intervals as function of solar radius, ion-inertial scale f_{di} (red), ion gyroscale f_{ρ_i} (orange), cyclotron resonant scale f_{Ω} (blue). Additionally a correction to the Taylor Hypothesis approximation to the cyclotron scale f'_{Ω} (green). Break points from spectral fits are also shown f_{IT} (black) and f_{TK} (teal). The gyrofrequency $\Omega/2\pi$ is shown in purple. b) Histograms show the distribution of frequency ratios f_{di}/f_{IT} (red), f_{Ω}/f_{IT} (blue), f'_{Ω}/f_{IT} (green) and f_{ρ_i}/f_{TK} (orange).

with the solar surface, sampling a relatively singular source region over the range of 14-55 R_{\odot} (Badman et al. 2023; Davis et al. 2023). We use measurements from the PSP Solar wind Electron Alpha and Proton experiment’s Solar Probe Analyzer (Livi et al. 2022, SPAN). The PSP FIELDS experiment (Bale et al. 2016) provides measurements of the magnetic field from DC to sub-ion kinetic scales using merged search coil (Jannet

et al. 2021) and fluxgate magnetometer (SCaM) measurements (Bowen et al. 2020d).

We break the 4 day stream into a set of intervals of 128 s with 50% overlap to study the evolution of the turbulent spectra alongside ion-scale waves. SCaM data are sensitive well into the sub-ion kinetic scales (Dudok de Wit et al. 2022), but are only available for two axes; as a result, the SCaM data are only used to measure the shape of the spectra. The fluxgate magnetometer data provides three component magnetic field measurements that enable comprehensive study of the properties of observed waves. The fluxgate magnetometer and SCaM data are re-sampled to a uniform 146.4845 Sa/sec rate. Data were discarded when discontinuities or changes in instrumental modes led to artifacts. In total 6737 intervals of 128 s were analyzed.

Turbulent Spectra—We compute spectral densities $E(f)$, with units nT^2/Hz , from the two-component SCaM data through ensemble averaging over 4096 point FFTs in each 128s interval. Each spectral density is interpolated onto 320 logarithmically spaced frequencies. Figure 1(a) shows spectral densities computed from the stream intervals, though for clarity only every 40th spectra is plotted. The colors corresponding to radial distance from the sun, which is between 14.1-55.0 R_{\odot} ; lighter yellow colors are closer to the Sun, whereas darker colors correspond to further heliocentric distances.

An estimate of the local spectral index for each frequency is obtained by performing a linear least-square fit of $\log_{10}E(f)$ in a moving window consisting of 60 neighboring logarithmically spaced frequencies. The slope of a linear least-square fit in log space provides a measure of the local spectral index $\alpha(f)$. Figure 1(b) shows the locally measured α as a function of frequency for spectra in Figure 1(a). The observed spectra are consistent with three-power-law spectra often reported in the solar wind (Sahraoui et al. 2009; Alexandrova et al. 2008; Bowen et al. 2020c): each spectra has a characteristic low-frequency inertial range scaling α_I , a transition range with steepened index α_T , followed by flattening to an index α_K at higher frequencies. The shape of the spectra is consistent but shifts to higher frequencies closer to the Sun. The index of the steep transition range spectra varies, and can have values of up to -10. The extremely steep transition range indices in this stream are predominantly associated with parallel spectra as shown in Duan et al. (2021). As we demonstrate, this steepening is also associated with significant ICW populations (Bowen et al. 2020a, 2023).

To determine the slope of the transition range α_T we implement a piecewise, three power-law (3PL) fit, following methods developed in Bowen et al. (2020c). Each

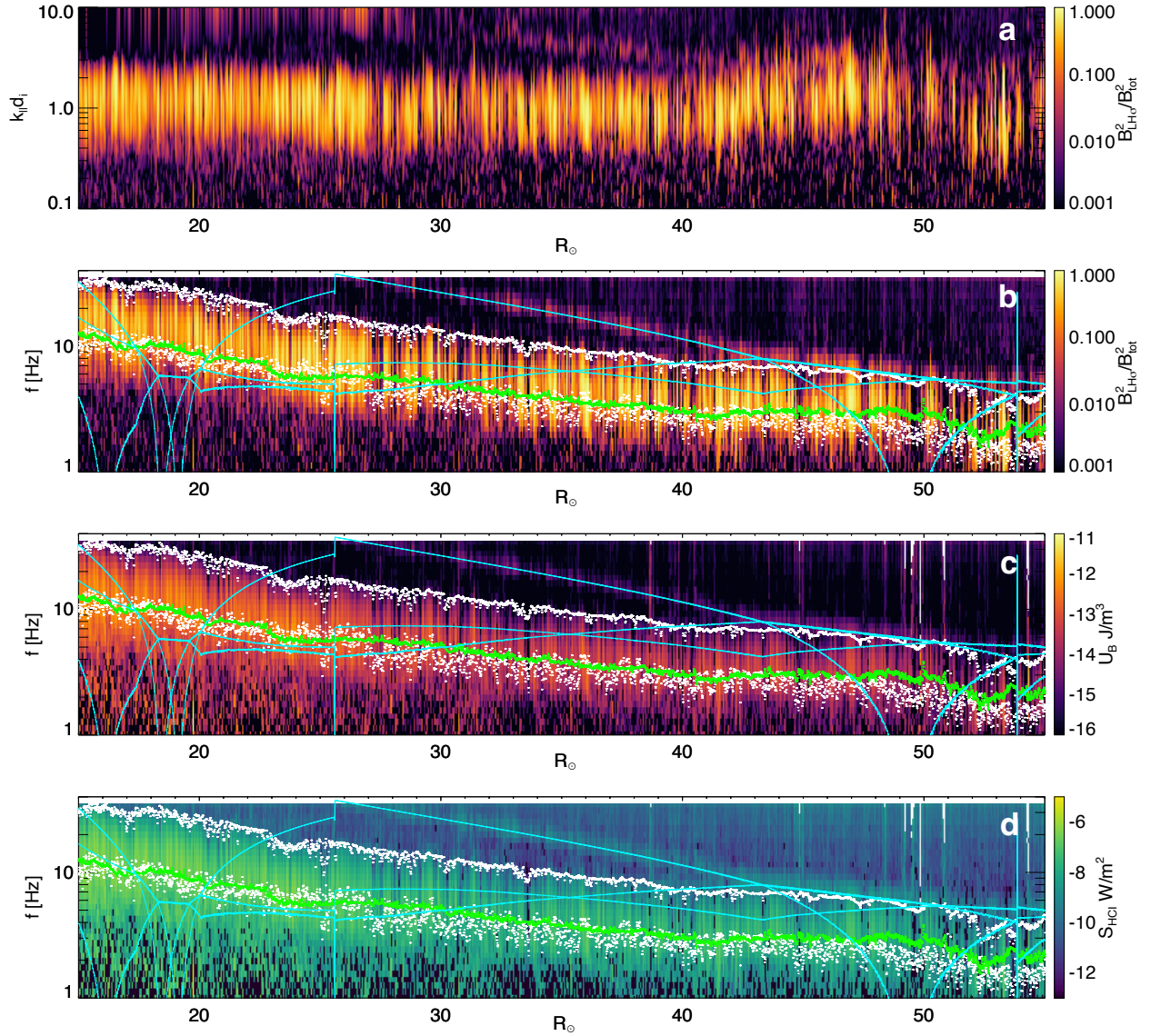


Figure 3. a) Fractional left-handed power $\tilde{B}_{LH\sigma}^2/\tilde{B}_{total}^2$ computed from wavelet-transform for each of the 6737 intervals as a function of $k_{\parallel}d_i$. b) Spectrogram of left-handed circularly polarized power as function of radial distance; f_{IT} and f_{TK} for each measurement are plotted in white, as well as the cyclotron scale f_{Ω} in green; teal lines show frequencies corresponding to spacecraft reaction wheels (Bowen et al. 2020a). c) internal energy U_B and d) Poynting flux of waves in a heliocentric inertial frame S_{HCI} computed from the cold-plasma dispersion relation.

of the three ranges is modeled as a power-law spectra with indices α_I , α_T , and α_K separated by break-point frequencies f_{IT} and f_{TK} , referring to the respective inertial-transition and transition-kinetic breaks. Fig. 1(c) shows the 3PL fits, corresponding to the spectra in Figure 1(a). Additionally, we apply the procedure to measure the local spectral index $\alpha(f)$ to the 3PL-fits, with the results shown in Figure 1(d). There is good agreement between the observations and the 3PL fits.

Break Scales & Cyclotron Resonance—We compare the measured break scales f_{IT} and f_{TK} to various physical ion-kinetic scales: the ion gyroradius, $\rho_i = v_{thi}/\Omega_i$,

where the ion thermal speed is $v_{thi} = \sqrt{2k_B T_i/m_i}$ and the ion gyrofrequency is $\Omega_i = eB_0/m_i$; and the ion inertial scale $d_i = \rho_i/\sqrt{\beta_i}$, where $\beta_i = 2n_0\mu_0 T_i/B_0^2$. The fundamental charge is given as e , μ_0 is the permeability of free space, T_i is the proton temperature, B_0 is the average background magnetic field, n_0 is the background number density. The wavenumbers corresponding to the ion-inertial and ion gyroscale are $k_{\rho_i} = \rho_i^{-1}$ and $k_{d_i} = d_i^{-1}$. We approximate the wavenumber corresponding to cyclotron resonant interactions as $k_{\Omega} = \Omega_i/(v_A + v_{thi})$, where v_A is the Alfvén speed $v_A = B_0/\sqrt{\mu_0 m_i n_0}$ (Leamon et al. 1998; Wicks et al. 2016; Woodham et al.

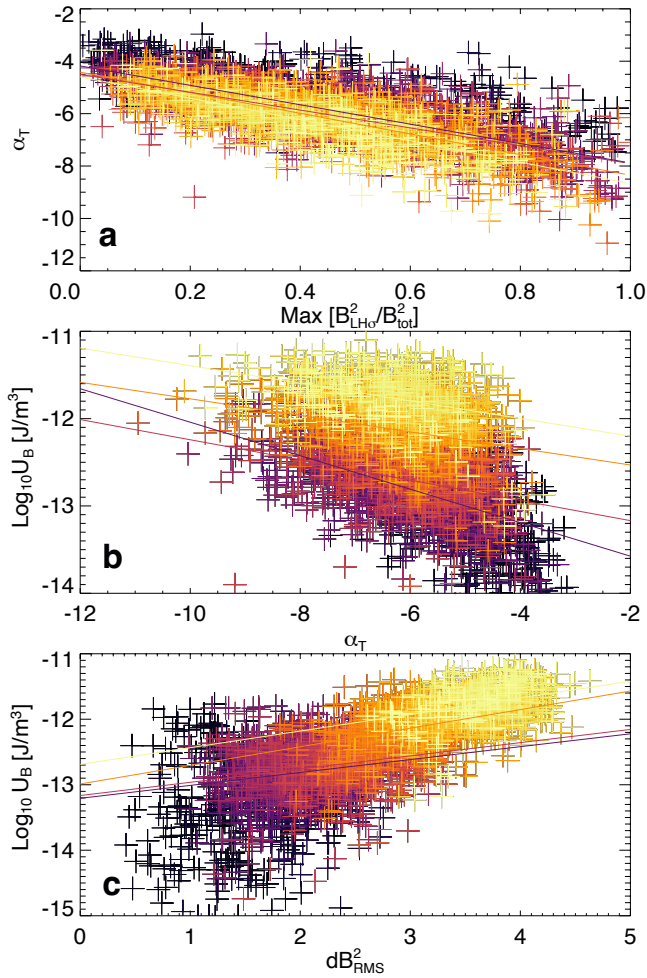


Figure 4. a) Transition range spectral index α_T against maximum circular polarization $\max[\tilde{B}_{LH\sigma}^2/\tilde{B}_{total}^2]$. b) Total internal energy of cyclotron waves U_B plotted against α_T . c) Total internal energy of cyclotron waves U_B , which is bandwidth limited and filtered by left hand polarization at ion-kinetic scales, plotted against total rms amplitude of magnetic field dB_{rms}^2 computed at 128 seconds. Data are colored by R_\odot with larger heliocentric distances in darker shades. Solid lines show the linear regression for 10 – 20 R_\odot (yellow), 20–30 R_\odot (orange), 30–40 R_\odot (red), and 40–50 R_\odot (purple), darker colors correspond to larger distances.

2018; Bowen et al. 2020a). This approximation for k_Ω is derived via the cyclotron resonance condition between outward going ICW and protons flowing inwards in the plasma frame, $\omega + k_\parallel v_{th} = \Omega_i$ (Leamon et al. 1998), and a low frequency limit $\omega = k_\parallel v_A$ to the ion-cyclotron dispersion for parallel propagating waves. The cold-plasma dispersion relation is

$$\left(\frac{\omega_{ICW}}{\Omega_i}\right)^2 = \left[\frac{k_\parallel d_i}{2} \left(\sqrt{k_\parallel^2 d_i^2 + 4} - k_\parallel d_i\right)\right]^2. \quad (1)$$

For the ion-scales k_{d_i} , k_{ρ_i} , and k_Ω , each wavenumber is converted to an effective spacecraft frequency f first using the Taylor hypothesis, $2\pi f \approx kv_{sw}$ to associate ion-kinetic scales with spacecraft frequencies f_{d_i} , f_{ρ_i} , and f_Ω . For the cyclotron-resonant scale, k_Ω , we also consider a correction to the Taylor hypothesis made by incorporating the Doppler shift equation

$$2\pi f = \omega(k) + \mathbf{k} \cdot \mathbf{v}_{sw}, \quad (2)$$

to improve on our estimate of the frequency corresponding to cyclotron resonant interactions as

$$2\pi f'_\Omega = \omega_{ICW}(k_\Omega) + k_\Omega v_{sw}, \quad (3)$$

which includes the contribution from ω_{ICW} evaluated at k_Ω . For calculating f'_Ω , we assume that the angle between the mean magnetic field and flow direction, θ_{BV} , is small such that $\cos\theta_{BV} \approx 1$ and thus $\mathbf{k} \cdot \mathbf{v}_{sw} \approx k_\Omega v_{sw}$ for parallel propagating ICWs.

Fig. 2(a) shows the computed kinetic-scale frequencies alongside the measured breaks from the 3PL fitting algorithm against R_\odot . Fig. 2(b) shows distributions ratios of f_{d_i}/f_{IT} , f_Ω/f_{IT} , f'_Ω/f_{IT} and f_{ρ_i}/f_{TK} . These distributions provide a measure of agreement between break frequencies and the measured ion kinetic scales. Recent work has suggested that the cyclotron scale f_Ω corresponds well with f_{IT} (Woodham et al. 2018; Vech et al. 2018; Duan et al. 2020; Lotz et al. 2023), here we find that f_Ω is statistically lower than f_{IT} ; however, the corrected f'_Ω frequency well approximates the f_{IT} break. The f_{IT} transition range break additionally approximates f_{d_i} , such that we cannot distinguish the inertial scale from the cyclotron resonant scale. We find that f_{ρ_i} is within the transition range, which is consistent with previous results (Bowen et al. 2020c).

Importantly, f_Ω and f'_Ω are estimates to a single cyclotron resonant scale corresponding to resonance between particles at the thermal speed v_{th} , with low-frequency ICWs, $\omega = kv_A$. However, observations from the solar wind suggest that ICWs occur over a range of frequencies corresponding to $kd_i \approx 1$ (Bowen et al. 2020a). Empirical determination of circular polarization as a function of spacecraft frequency along with the cold plasma dispersion for parallel propagating ICWs Eq. (1) provides information regarding the wavenumbers at which cyclotron resonant waves occur (Bowen et al. 2020b).

A 64-scale Morlet wavelet transform is applied to each interval to compute a power spectral density $\tilde{B}^2(f, t)$ with units nT^2/Hz (Farge 1992; Dudok de Wit et al. 2013; Bowen et al. 2020a). We extract circular polarization of the field via the reduced magnetic-helicity (Howes

& Quataert 2010),

$$\sigma_B(f, t) = -2\text{Im}(\tilde{B}_{\perp 1}\tilde{B}_{\perp 2}^*)/(\tilde{B}_{\perp 1}^2 + \tilde{B}_{\perp 2}^2). \quad (4)$$

of the wavelet coefficients perpendicular to the mean field with left/right handed polarization represented by positive/negative σ_B . We calculate the left-handed polarized power spectra $\tilde{B}_{LH\sigma}^2$ by filtering out power with $\sigma_B < 0.9$. The normalized fractional left handed spectra are computed as $\tilde{B}_{LH\sigma}^2/\tilde{B}_{total}^2$. Very little right handed polarization is present in this stream.

Based on previous measurements of the phase speed of circularly polarized waves (Bowen et al. 2020b), which show a strong statistical preference for outward-propagation, we can assume that the waves are outward-propagating ICWs, travelling parallel to the mean field. The wavelet transform gives circular polarization as a function of the spacecraft frame frequency, f . The use of the Doppler shift Eq. (2) in the parallel-propagating limit gives

$$2\pi f = \omega_{ICW} \pm k_{\parallel} v_{sw} \cos\theta_{BV}, \quad (5)$$

where we no longer assume either the Taylor Hypothesis or that $\cos\theta_{BV} \approx 1$. The combination of Eq. (5) with Eq. (1) determines the corresponding parallel wavenumber k_{\parallel} for each spacecraft frequency f (Bowen et al. 2020b). Figure 3(a) shows the normalized $\tilde{B}_{LH\sigma}^2/\tilde{B}_{total}^2$ as function of $k_{\parallel}d_i$ computed from combining Eq. (1) with Eq. (5). At all radial distances the ICW population appears at $k_{\parallel}d_i = 1$, where ICWs are inherently dispersive, with a finite bandwidth in wave number ranging from approximately $k_{\parallel}d_i \sim 0.3 - 4$. The finite bandwidth indicates that, at each time, a range of particle velocities simultaneously satisfy the ICW resonance condition. It is important to note that the spacecraft reaction wheels, highlighted in teal lines in Figure 3(b-d), contribute circularly polarized power at higher $k_{\parallel}d_i$ (Bowen et al. 2020a).

Fig. 3(b) shows $\tilde{B}_{LH\sigma}^2/\tilde{B}_{total}^2$ as a function of spacecraft frequency at each interval studied as a function of solar radial distance. We plot both the f_{IT} and f_{TK} breaks. The f_{IT} break agrees very well with the circularly polarized regime, while the f_{TK} break bounds the circular polarization at higher frequencies, indicating that the transition range is entirely circularly polarized. We additionally plot the cyclotron scale f_{Ω}^* , which approximates the f_{IT} break.

Cyclotron Waves and Turbulent Dissipation—Using the cold-plasma dispersion and the Doppler shift Eqs. (1) & (2) and our observations of $\tilde{B}_{LH\sigma}^2(k_{\parallel}d_i)$ we measure both the internal energy density of the waves U_B and the magnitude of the Poynting flux computed in an Heliocentric inertial frame (HCI), S_{HCI} assuming the ICW

propagation is entirely parallel the radial solar wind flow (Karpman 1974; Shklyar & Matsumoto 2009):

$$U'_B = \frac{\tilde{B}_{LH\sigma}^2 v_{ph}}{\mu_0 v_g} = \frac{\tilde{B}_{LH\sigma}^2 (2\Omega_i - \omega)}{2\mu_0 (\Omega_i - \omega)}, \quad (6)$$

$$S'_{HCI} = (v_{sw} + v_g)U'_B, \quad (7)$$

where v_{ph} and v_g are the plasma frame phase and group velocities respectively. As the units of $\tilde{B}_{LH\sigma}^2$ are nT^2/Hz both U'_B and S'_{HCI} are defined as spectral densities. The internal energy U_B and Poynting flux magnitude S_{HCI} corresponding to each wavelet coefficient are obtained by multiplying U'_B and S'_{HCI} by the bandwidth of each wavelet $\Delta f = \frac{df}{dk_{\parallel}} \Delta k_{\parallel}$, where the derivative df/dk_{\parallel} and Δk_{\parallel} are obtained from Eq. 5. Figure 3 (c&d) show U_B and S_{HCI} at each frequency over the interval.

The total Poynting flux and internal energy can be integrated at each time to give total values U_{tot} and S_{tot} for each interval. Due to the sporadic noise that occurs at low frequencies, as well as high frequency contributions to polarization from the spacecraft reaction wheels, we zero out contributions to S_{tot} and U_{tot} where $kd_i < 0.3$ and $kd_i > 5$.

We use U_{tot} and $B_{LH\sigma}^{\max} = \max[\tilde{B}_{LH\sigma}^2/\tilde{B}_{total}^2]$ as proxies for the ICWs in each interval. Fig. 4 shows how these quantities relate to parameters associated with turbulence, α_T and as well as the total RMS turbulent amplitude $\langle \delta B^2 \rangle$ computed in each 128 s interval. We consider only intervals with $150^\circ < \theta_{BV} < 170^\circ$ in order to control for effects associated with anisotropy, which affect observational signatures of both the waves and the turbulence (Chen et al. 2010; Bowen et al. 2020a); of the total 6736 intervals, 3172 occur with $150^\circ < \theta_{BV} < 170^\circ$. In each panel of Fig. 4 data is plotted with the color scale in Fig. 1 with lighter colors corresponding to intervals closer to the sun. We compute lines of best fit for data within $10 - 20R_{\odot}$, $20 - 30R_{\odot}$, $30 - 40R_{\odot}$, and $40 - 50R_{\odot}$, which are shown in each panel of Fig. 4. Fig. 4(a) shows that the transition range slope α_T is strongly correlated with the level of circular polarization, $B_{LH\sigma}^{\max}$ (Bowen et al. 2023), with similar trends observed at all solar radii. Fig. 4(b) shows that the internal energy of the waves U_B is anti-correlated with α_T , such that steeper slopes contain greater amounts of ICW energy. This correlation is present at all R_{\odot} , though at larger distances the maximum measured U_{tot} are similar to the lowest U_{tot} close to the sun, such that constraining the data by R_{\odot} is necessary to see the correlations. Fig. 4(c) shows that the internal energy contained within the circularly polarized ion-scale transition range is globally a function of the amplitude of the turbulent fluctuations

dB_{rms}^2 computed at the 128 s scale, consistent with previous results in Shankarappa et al. (2023).

ICW Heating Rates—Our analysis of the transition range reveals signatures of circularly polarized ion-cyclotron resonant waves; we apply well established principles of energy conservation and quasilinear heating to connect these waves to turbulent dissipation.

The Poynting theorem states that the change in internal energy of the ICW population is

$$\frac{\partial U_B}{\partial t} = -\nabla \cdot \mathbf{S} - Q_{ICW} + \epsilon_{ICW}, \quad (8)$$

where Q_{ICW} is the dissipation rate of the waves and ϵ_{ICW} is a driving term. Assuming a steady state, we compute the three terms on the right side of Eq. (8). We approximate $\nabla \cdot \mathbf{S}$ in the heliocentric inertial frame as the radial derivative

$$\nabla \cdot \mathbf{S} \approx \frac{1}{r^2} \frac{\partial}{\partial r} r^2 S_{tot}. \quad (9)$$

We estimate Q_{ICW} using the quasilinear heating rate (Kennel & Engelmann 1966) with the empirically observed spectrum of cyclotron waves

$$I(k_{\parallel}) = \frac{\tilde{B}_{LH\sigma}^2}{B_0^2} \frac{df}{dk_{\parallel}}. \quad (10)$$

For each SPANi measurement, we perform a drifting bi-Maxwellian fit in the proton core frame with the form

$$g_p(v_{\perp}, v_{\parallel}) = \frac{n_c}{\pi^{3/2} w_{c,\perp}^2 w_{c,\parallel}} \exp \left[-\frac{v_{\perp}^2}{w_{c,\perp}^2} - \frac{v_{\parallel}^2}{w_{c,\parallel}^2} \right] + \frac{n_b}{\pi^{3/2} w_{b,\perp}^2 w_{b,\parallel}} \exp \left[-\frac{v_{\perp}^2}{w_{b,\perp}^2} - \frac{(v_{\parallel} - v_D)^2}{w_{b,\parallel}^2} \right], \quad (11)$$

which has anisotropic thermal speeds perpendicular and parallel the mean field (\perp and \parallel) for the beam and core (subscripts, b and c): $w_{c,\perp}$, $w_{c,\parallel}$, $w_{b,\perp}$, $w_{b,\parallel}$ and a relative drift, v_D , parallel to the mean magnetic field (Marsch 2006; Klein et al. 2021). We compute the average fit parameters over the 128s interval such that an average gyrotropic $\bar{g}(v_{\perp}, v_{\parallel})$ is computed. Using $\bar{g}(v_{\perp}, v_{\parallel})$, and the observed spectrum of cyclotron waves $I(k_{\parallel})$, we use the cold plasma dispersion, Eq. 1, with wave numbers defined from Eq. 5, to determine the volumetric heating rate in the local interval:

$$Q_{ICW} = \int \frac{m_p v^2}{2} \frac{\partial \bar{g}}{\partial t} d^3 \mathbf{v} = \frac{\pi e^2}{4m_p} \int d^3 \mathbf{v} \left\{ v^2 \int_0^{\infty} dk_{\parallel} \frac{1}{v_{\perp}} \hat{G}_k \left[v_{\perp} \delta(\omega_k - k_{\parallel} v_{\parallel} - \Omega_p) \times \frac{\omega_k^2}{k_{\parallel}^2 c^2} I(k_{\parallel}) \hat{G}_k \bar{g}(v_{\perp}, v_{\parallel}) \right] \right\}, \quad (12)$$

with

$$\hat{G}_k = \left(1 - \frac{k_{\parallel} v_{\parallel}}{\omega_k} \right) \frac{\partial}{\partial v_{\perp}} + \frac{k_{\parallel} v_{\perp}}{\omega_k} \frac{\partial}{\partial v_{\parallel}} \quad (13)$$

(Kennel & Engelmann 1966). A gyrotropic differential volumetric heating rate $Q(v_{\perp}, v_{\parallel})$ can be defined from $Q_{ICW} = \int Q(v_{\perp}, v_{\parallel}) dv_{\parallel} dv_{\perp}$. We outline how to calculate Q_{ICW} and $Q(v_{\perp}, v_{\parallel})$ in Appendix A through using the δ -function to evaluate the integral over wave number and the subsequent numerical integration of $Q(v_{\perp}, v_{\parallel})$ over velocity coordinates.

Figure 5(a-b) shows $Q(v_{\parallel})$, the volumetric heating rate as function of resonant parallel velocity, which is computed from integrating $Q(v_{\perp}, v_{\parallel})$ over perpendicular velocities, as a function of solar radius. Figure 5(a) shows positive $Q(v_{\parallel}) \Delta v_{\parallel}$, at resonant velocities less than the thermal speed (shown in yellow), corresponding to wave-absorption and consequent plasma heating. The Δv_{\parallel} term, which is the resolution of the numerical integration 1 km/s, is included to normalize the differential $Q(v_{\parallel})$ in terms of a volumetric heating rate W/m³. Figure 5(b) shows wave emission, which, consistent with Bowen et al. (2022), is significantly less energetically relevant than the regions with positive $Q(v_{\parallel}) \Delta v_{\parallel}$ wave-absorption, which indicates net resonant-heating of the plasma.

Importantly, the use of a biMaxwellian model to approximate the distribution may not capture non-thermal features that resonate with the observed populations of waves (Dum et al. 1980; Viñas & Gurgiolo 2009). In Appendix B, we implement two well understood non-parametric techniques to model the observed distributions, Hermite polynomials and radial basis functions, to verify the independence of our results from the bi-Maxwellian model. While there are slight differences in the level of heating predicted by each model, the qualitative interpretation of ICW resonance heating is found in each case and the average values closely follow that of the drifting biMaxwellian.

Connecting ICW Heating to the Turbulent Cascade—The importance of resonant heating can be understood by

comparing the net heating rates Q_{ICW} to the turbulent cascade rate ϵ . Following (Bandyopadhyay et al. 2020) we compute the energy cascade rate of the turbulence assuming a von Kármán decay law.

$$\epsilon'^{\pm} = \alpha \frac{(\delta z^{\pm})^2 \delta z^{\mp}}{L^{\pm}}, \quad (14)$$

where δz^{\pm} are root mean square fluctuation amplitudes of the Elsasser variables $\delta \mathbf{z}^{\pm} = \delta \mathbf{v} \pm \delta \mathbf{B} / \sqrt{\mu_0 \rho}$. The correlation length L^{\pm} is determined from the solar-wind advected spatial-scale corresponding to the time-lag for which the correlation reduces below a factor e^{-1} . The coefficient $\alpha = 0.03$ is determined from numerical means (Hossain et al. 1995; Wan et al. 2012; Usmanov et al. 2014; Bandyopadhyay et al. 2018) and chosen to agree with Bandyopadhyay et al. (2020) and Wu et al. (2022). However, this value of α is derived assuming low cross helicity, while the near-Sun solar wind is characterized by imbalance with $\sigma_c \approx 1$ (McManus et al. 2020). Note the units for ϵ' in equation 14 are of J/s/kg; we define ϵ with units of W/m³, which are comparable to the volumetric heating rates in Equation 12, through multiplying ϵ' by the background mass density $\epsilon = \epsilon' m_i n_0$.

Measurement of ϵ'^+ via Eq. (14), which we assume approximates the total cascade rate ϵ' , requires the Elsasser amplitude δz^{\pm} at the outer, energy containing scales, of the turbulence. Davis et al. (2023) have studied the evolution of the outer scales in this same stream and found that the outer-scale spectral break evolves from 10^{-2} Hz close to $14 R_{\odot}$ to 10^{-3} Hz at $\sim 50 R_{\odot}$. Accordingly, we compute the cascade rate ϵ'^+ in successive 30 minute intervals (corresponding to $\approx 5 \times 10^{-4}$ Hz) with 50% overlap. In each 30 minute interval we then compute the average heating rate $\langle Q_{\text{ICW}} \rangle$ and $\langle \nabla \cdot \mathbf{S} \rangle$.

Figure 5(c) shows ϵ , $\langle Q_{\text{ICW}} \rangle$ and $\langle \nabla \cdot \mathbf{S} \rangle$ as a function of radial distance. A surprisingly good agreement is found between ϵ and $\langle Q_{\text{ICW}} \rangle$, while the divergence of the Poynting flux term is significantly smaller. The relatively small $\langle \nabla \cdot \mathbf{S} \rangle$ indicates that the wave dynamics are dominated by the source, ϵ_{ICW} , and dissipation, Q_{ICW} , and that the waves do not propagate significantly. This result is consistent with previous studies arguing for in situ driving of these waves (Bowen et al. 2020a; Vech et al. 2020; Liu et al. 2023).

We find a Spearman, non-parametric, ranked correlation between ϵ and $\langle Q_{\text{ICW}} \rangle$ of 0.79; we further compute the Pearson-correlation of the logarithmic quantities as 0.88. Both of these values indicate strong correlations. Furthermore, we fit each of ϵ and $\langle Q_{\text{ICW}} \rangle$ to a power-law in R_{\odot} noted as ϵ' and Q'_{ICW} . We compute the local variations from the global power-law trends using $\epsilon - \epsilon'$ and $\langle Q_{\text{ICW}} \rangle - Q'_{\text{ICW}}$ as a measure of how closely the local quasilinear heating rate follows the turbulent energy

cascade rate. Figure 5(d) shows the local fluctuations $\langle Q_{\text{ICW}} \rangle - Q'_{\text{ICW}}$ against $\epsilon - \epsilon'$. We measure a Spearman ranked-correlation of 0.56.

Additionally, we interpolate ϵ , measured at a 30 minute cadence, onto the 128 second cadence of the Q_{ICW} measurements. Figure 5(e) shows a 2D-histogram of Q_{ICW} against the interpolated ϵ ; the distribution is column-normalized to the measured cascade rate. Good correlations are obtained, with a Spearman ranked-correlation of 0.58. These results suggest that characteristically, the quasilinear heating rate is proportional to the energy cascade rate with a constant of proportionality near unity. Figure 5(f) shows a 2D-histogram of Q_{ICW}/ϵ , where the interpolated ϵ is again used, against solar radius R_{\odot} ; the distribution is column-normalized to R_{\odot} . Implicitly, this suggests that much of the turbulent cascade flux enters the ICW population such that $Q_{\text{ICW}} = \chi \epsilon'$ with $\chi \approx 0.1 - 1$ over the vast majority of the observed stream. There is some radial trend, with $0.1 < \chi < 0.5$ at $\approx 15 - 20 R_{\odot}$ and $\chi \approx 1$ at larger distances. Values with $\chi > 1$ suggest dissipation in excess of the turbulent cascade rate, we believe this is predominantly due to uncertainty in the measurements of Q_{ICW} and ϵ .

3. CONCLUSIONS

The nature of the steepening of turbulent energy spectrum at ion-kinetic scales has long been debated and is an important signature in understanding collisionless turbulent dissipation (Denskat et al. 1983; Smith et al. 1990; Goldstein et al. 1994; Leamon et al. 1998). Studies of the location of the ion-kinetic scale break frequency suggest that the most likely candidate scale corresponds to resonance between outward going ICWs and the thermal ion population (Woodham et al. 2018; Vech et al. 2018; Duan et al. 2020; Lotz et al. 2023). Previous observations from 1 AU have suggested that ICW play a role in dissipating solar wind turbulence (Leamon et al. 1998; Lion et al. 2016; Woodham et al. 2019; Telloni et al. 2019; Zhao et al. 2021; Luo et al. 2022). In this Letter, we concretely demonstrate that ion-scale spectral steepening is associated with circular polarization. The break between the inertial and transition ranges follows the regime of ICWs, and the spectral break between the transition range and subion-scale turbulence bounds the circularly polarized waves exactly at higher frequencies. We suggest that the transition range corresponds to cyclotron waves that are associated with turbulent dissipation and ion-scale heating (Bowen et al. 2023). Our results show that internal energy and momentum of the waves is correlated with the amplitude of the turbulent fluctuations, Figure 3, suggesting that the energy

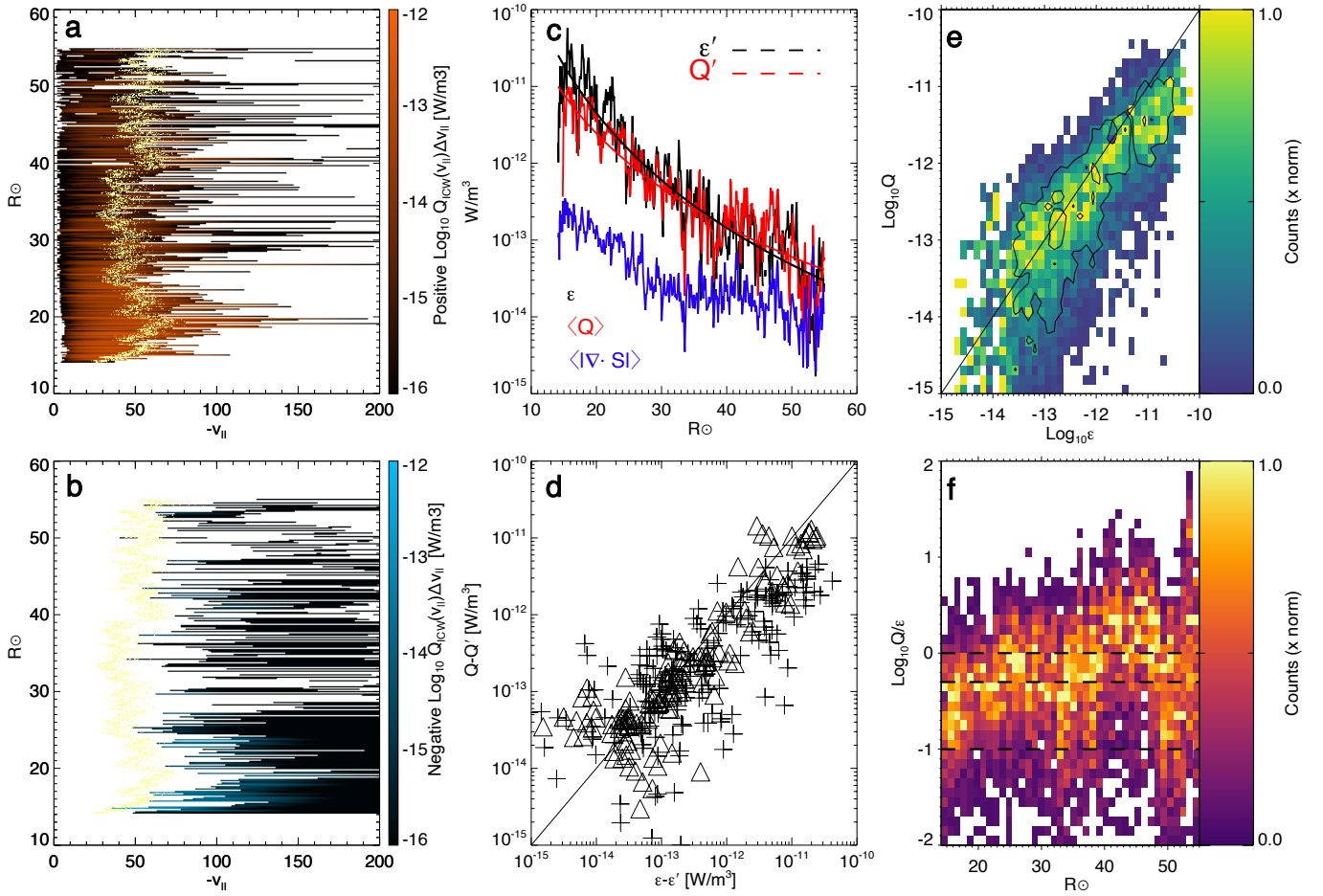


Figure 5. a) Volumetric heating rates, $Q(v_{\parallel})\Delta v_{\parallel}$, with $\Delta v_{\parallel} = 1\text{km/s}$, which have been integrated over perpendicular velocity, as a function of resonant parallel velocity and solar radial distance. b) Same as panel a, but for negative values of $Q(v_{\parallel})\Delta v_{\parallel}$. Yellow dots in panels a& b show the measured parallel thermal speed. c) Measured turbulent cascade rate ϵ from von Kármán decay law (black), average cyclotron heating rate from quasilinear theory $\langle Q_{ICW} \rangle$ (red), and $\langle \nabla \cdot \mathbf{S} \rangle$ for total cyclotron waves (blue). Power-law fits, ϵ' and Q_{ICW}' , are shown in dashed lines. d) $\langle Q_{ICW} \rangle - Q_{ICW}'$ plotted against $\epsilon - \epsilon'$, where + and Δ corresponds to data with $\langle Q_{ICW} \rangle - Q_{ICW}'$ and $\epsilon - \epsilon'$ respectively greater and less than zero. e) Two-dimensional histogram of Q_{ICW} against ϵ interpolated onto 128 second cadence. f) Two-dimensional histogram of Q_{ICW}/ϵ against R_{\odot} ; dashed black lines show Q_{ICW}/ϵ at levels of 0.1, 0.5, and 1; the average value of Q_{ICW}/ϵ is shown in black; $Q_{ICW}/\epsilon > 1$ indicating quasilinear heating at levels greater than the turbulent cascade may arise due to uncertainty in the estimates of both Q_{ICW} and ϵ . The distributions in panels e&f are column normalized to the maximum value in each data column.

contained in, and transported by, the waves originates from the turbulent fluctuations. These results are consistent with earlier observations from 1 AU suggesting that the level of steepening in the turbulent cascade may relate to the level of Alfvénicity and the turbulent cascade rate (Smith et al. 2006; Bruno et al. 2014).

In this Letter, we compute two measures of energy transfer: first, the quasilinear heating rate of kinetic scale ICWs, $\langle Q_{ICW} \rangle$, and second, the von Kármán turbulent decay rate ϵ^+ . The measurements of $\langle Q_{ICW} \rangle$ are obtained through integrating kinetic phase space densities measured by SPANi, while ϵ^+ is determined from outer scale turbulent fluctuations. It is striking that these quantitative estimates of energy transfer, ϵ^+

and Q_{ICW} , obtained via entirely different methods at vastly different spatial scales show significant correlations. Such strong correlations suggest that parallel-cyclotron resonance dissipates significant amounts of turbulent energy into the solar-wind ion populations. The correlation between energy flux and quasilinear heating rate is observed in both the global scaling of the quantities as well as in local variations: i.e., fluctuations in the turbulent cascade rate are typically accompanied by correlated variations in the quasilinear heating rate. These novel measurements, which support a radially extended cyclotron heating mechanism, are important in understanding how turbulent dissipation results in heating the expanding solar wind. These results further in-

dicating significant progress on PSP’s objective “to trace the flow of energy that heats and accelerates the solar corona and solar wind” (Fox et al. 2016). Furthermore, the extended ICW heating, which is observed from 15 to 55 R_{\odot} , may have significant implications for the role of ICW heating in the corona, (Hollweg & Johnson 1988; Cranmer 2000).

Recent simulations by Squire et al. (2022) suggest that the dissipation of strongly imbalanced Alfvénic turbulence may result in polarization signatures similar to those measured in the solar wind (Podesta & Gary 2011; He et al. 2011; Huang et al. 2020). The Squire et al. (2022) simulations, and the underlying idea of a helicity barrier whereby imbalanced turbulence is prevented from cascading to small scales due to a conserved generalized helicity (Meyrand et al. 2021), provides a novel framework to understand the connection between turbulence and ion-cyclotron waves. These theoretical ideas have found support in observations showing that ion-scale ICWs preferentially occur when large-scale fluctuations are highly Alfvénic (Bowen et al. 2023) and that sub-ion scale intermittency depends largely on the level of ICWs present, which is in turn correlated to the cross-helicity, suggesting that ICWs play a role in the dissipation of imbalanced turbulence.

The idea that parallel propagating ICWs dissipate a predominantly perpendicular cascade challenges our current understandings of solar wind turbulence and dissipation. It has long been suggested that the turbulence should drive fluctuations into smaller perpendicular scales (Shebalin et al. 1983), and observations regularly indicate significant anisotropy perpendicular the mean field (Horbury et al. 2008; Chen et al. 2010; Duan et al. 2021). The hybrid simulations of the helicity barrier by Squire et al. (2022) suggest that oblique ICWs are the primary heating mechanism and that parallel ICWs are emitted as a secondary process (Chandran et al. 2010) through the Alfvén/ion cyclotron instability (Gary 1993).

While the secondary emission of parallel ICWs from oblique-ICW heating provides a mechanism to generate parallel ICWs from turbulent heating, in such a mechanism, the plasma is heated by oblique ICWs but cooled by the parallel ICWs (since they are emitted as an instability). In contrast, our measurements indicate that the parallel ICWs are robustly heating the plasma, suggesting they should be directly driven by the turbulence, as opposed to generated via oblique ICW heating. If our present measurements, consistent with previous observations (Bowen et al. 2022), are correct, this presents a conundrum, given the difficulty of sourcing quasi-parallel waves from perpendicular turbulent structures. Our use

of non-parametric representations of $g(\mathbf{v})$ (Appendix B) further complicates this issue, as our measurement of ICW heating is not simply due to the incorrect parameterization of the SPANi observations with a drifting-bi-Maxwellian fit.

A possible source of systematic error is in the assumption of a cold-plasma. We assume a cold plasma dispersion (Stix 1992), that is likely not entirely accurate for the solar wind. Implementation of warm-plasma dispersion solvers with arbitrary distribution functions (Verscharen et al. 2017; Walters et al. 2023) may enable greater understanding of parallel wave-generation. Furthermore, inclusion of beam populations (Verniero et al. 2020; Ofman et al. 2022) and α -particles may affect instabilities (McManus et al. 2023) and may help further understanding of these dynamics.

Outside of uncertainties in the distribution function and wave-dispersion relations, a possible explanation for the in situ production of ICWs that result in solar wind heating could include the adiabatic evolution associated with expansion. Adiabatic evolution associated with expansion (Chew et al. 1956) should drive distribution functions that are unstable and emitting ICWs towards stability. The extent that expansion may enable ICW heating rather than cooling within the helicity-barrier framework, remains largely unstudied.

Furthermore, estimates of the cascade rate are notoriously difficult to estimate via single spacecraft measurements (Bandyopadhyay et al. 2018, 2020). Care must be taken in understanding these cascade rates, especially in strongly imbalanced states, in which a stationary energy flux may not exist, or a negative cascade rate may occur (Smith et al. 2009; Meyrand et al. 2021). This is especially important in the regime of imbalanced turbulence frequently observed by PSP (Meyrand et al. 2021; Squire et al. 2022). However, recently Wu et al. (2022) found good agreement between the Von Kármán decay rates with measured perpendicular proton heating rates, suggesting that the turbulent dissipation can be studied via these methods. While care has to be taken in further studies of cascade rates, the general correspondence between the measured heating rates and the von Kármán decay rates obtained in this present work and by Wu et al. (2022) is promising.

In any case, these robust observations of extended cyclotron resonant process in the inner-heliosphere suggest that kinetic scale waves are strongly coupled to the turbulent cascade and provide an important pathway to the dissipation of turbulence in the solar wind and corona.

4. ACKNOWLEDGEMENTS

T.A.B. acknowledges NASA Grant No. 80NSSC24K0272. The work of I.V. was supported by NASA grant No. 80NSSC22K1634. B.D.G.C. acknowledges the support of NASA grant 80NSSC24K0171.

REFERENCES

- Alexandrova, O., Carbone, V., Veltri, P., & Sorriso-Valvo, L. 2008, *The Astrophysical Journal*, 674, 1153, doi: [10.1086/524056](https://doi.org/10.1086/524056)
- Badman, S. T., Riley, P., Jones, S. I., et al. 2023, arXiv e-prints, arXiv:2303.04852, doi: [10.48550/arXiv.2303.04852](https://doi.org/10.48550/arXiv.2303.04852)
- Bale, S., Badman, S., Bonnell, J., et al. 2019, *Nature*, 1
- Bale, S. D., Goetz, K., Harvey, P. R., et al. 2016, *Space Science Rev.*, 204, 49, doi: [10.1007/s11214-016-0244-5](https://doi.org/10.1007/s11214-016-0244-5)
- Bandyopadhyay, R., Oughton, S., Wan, M., et al. 2018, *Physical Review X*, 8, 041052, doi: [10.1103/PhysRevX.8.041052](https://doi.org/10.1103/PhysRevX.8.041052)
- Bandyopadhyay, R., Goldstein, M. L., Maruca, B. A., et al. 2020, *ApJs*, 246, 48, doi: [10.3847/1538-4365/ab5dae](https://doi.org/10.3847/1538-4365/ab5dae)
- Bavassano, B., Pietropaolo, E., & Bruno, R. 1998, *JGR*, 103, 6521, doi: [10.1029/97JA03029](https://doi.org/10.1029/97JA03029)
- Boardsen, S. A., Jian, L. K., Raines, J. L., et al. 2015, *Journal of Geophysical Research (Space Physics)*, 120, 10,207, doi: [10.1002/2015JA021506](https://doi.org/10.1002/2015JA021506)
- Bowen, T. A., Chandran, B. D. G., Klein, K. G., et al. 2023, in *2023 XXXVth General Assembly and Scientific Symposium of the International Union of Radio Science (URSI GASS)*, 335, doi: [10.23919/URSIGASS57860.2023.10265538](https://doi.org/10.23919/URSIGASS57860.2023.10265538)
- Bowen, T. A., Mallet, A., Huang, J., et al. 2020a, *ApJS*, 246, 66, doi: [10.3847/1538-4365/ab6c65](https://doi.org/10.3847/1538-4365/ab6c65)
- Bowen, T. A., Bale, S. D., Bonnell, J. W., et al. 2020b, *ApJ*, 899, 74, doi: [10.3847/1538-4357/ab9f37](https://doi.org/10.3847/1538-4357/ab9f37)
- Bowen, T. A., Mallet, A., Bale, S. D., et al. 2020c, *PRL*, 125, 025102, doi: [10.1103/PhysRevLett.125.025102](https://doi.org/10.1103/PhysRevLett.125.025102)
- Bowen, T. A., Bale, S. D., Bonnell, J. W., et al. 2020d, *Journal of Geophysical Research (Space Physics)*, 125, e27813, doi: [10.1029/2020JA027813](https://doi.org/10.1029/2020JA027813)
- Bowen, T. A., Chandran, B. D. G., Squire, J., et al. 2022, *PRL*, 129, 165101, doi: [10.1103/PhysRevLett.129.165101](https://doi.org/10.1103/PhysRevLett.129.165101)
- Broomhead, D., & Lowe, D. 1988, *Complex Systems*, 2, 321
- Bruno, R., Trenchi, L., & Telloni, D. 2014, *ApJL*, 793, L15, doi: [10.1088/2041-8205/793/1/L15](https://doi.org/10.1088/2041-8205/793/1/L15)
- Chandran, B. D. G., Pongkitiwanchakul, P., Isenberg, P. A., et al. 2010, *ApJ*, 722, 710, doi: [10.1088/0004-637X/722/1/710](https://doi.org/10.1088/0004-637X/722/1/710)
- Chen, C. H. K., Horbury, T. S., Schekochihin, A. A., et al. 2010, *Physical Review Letters*, 104, 255002, doi: [10.1103/PhysRevLett.104.255002](https://doi.org/10.1103/PhysRevLett.104.255002)
- Chew, G. F., Goldberger, M. L., & Low, F. E. 1956, *Proceedings of the Royal Society of London Series A*, 236, 112, doi: [10.1098/rspa.1956.0116](https://doi.org/10.1098/rspa.1956.0116)
- Cranmer, S. R. 2000, *The Astrophysical Journal*, 532, 1197, doi: [10.1086/308620](https://doi.org/10.1086/308620)
- . 2014, *ApJS*, 213, 16, doi: [10.1088/0067-0049/213/1/16](https://doi.org/10.1088/0067-0049/213/1/16)
- Davis, N., Chandran, B. D. G., Bowen, T. A., et al. 2023, arXiv e-prints, arXiv:2303.01663, doi: [10.48550/arXiv.2303.01663](https://doi.org/10.48550/arXiv.2303.01663)
- Denskat, K. U., Beinroth, H. J., & Neubauer, F. M. 1983, *Journal of Geophysics Zeitschrift Geophysik*, 54, 60
- Duan, D., He, J., Bowen, T. A., et al. 2021, *ApJL*, 915, L8, doi: [10.3847/2041-8213/ac07ac](https://doi.org/10.3847/2041-8213/ac07ac)
- Duan, D., Bowen, T. A., Chen, C. H. K., et al. 2020, *ApJS*, 246, 55, doi: [10.3847/1538-4365/ab672d](https://doi.org/10.3847/1538-4365/ab672d)
- Dudok de Wit, T., Alexandrova, O., Furno, I., Sorriso-Valvo, L., & Zimbardo, G. 2013, *SSRv*, 178, 665, doi: [10.1007/s11214-013-9974-9](https://doi.org/10.1007/s11214-013-9974-9)
- Dudok de Wit, T., Krasnoselskikh, V. V., Agapitov, O., et al. 2022, *Journal of Geophysical Research (Space Physics)*, 127, e30018, doi: [10.1029/2021JA030018](https://doi.org/10.1029/2021JA030018)
- Dum, C. T., Marsch, E., & Pilipp, W. 1980, *Journal of Plasma Physics*, 23, 91, doi: [10.1017/S0022377800022170](https://doi.org/10.1017/S0022377800022170)
- Farge, M. 1992, *Annual Review of Fluid Mechanics*, 24, 395, doi: [10.1146/annurev.fl.24.010192.002143](https://doi.org/10.1146/annurev.fl.24.010192.002143)
- Fox, N. J., Velli, M. C., Bale, S. D., et al. 2016, *Space Science Reviews*, 204, 7, doi: [10.1007/s11214-015-0211-6](https://doi.org/10.1007/s11214-015-0211-6)
- Gary, S. P. 1993, *Theory of Space Plasma Microinstabilities*
- Goldstein, M. L., Roberts, D. A., & Fitch, C. A. 1994, *Journal of Geophysical Research*, 99, 11519, doi: [10.1029/94JA00789](https://doi.org/10.1029/94JA00789)
- He, J., Marsch, E., Tu, C., Yao, S., & Tian, H. 2011, *The Astrophysical Journal*, 731, 85, doi: [10.1088/0004-637X/731/2/85](https://doi.org/10.1088/0004-637X/731/2/85)
- He, J., Wang, L., Tu, C., Marsch, E., & Zong, Q. 2015, *ApJ*, 800, L31, doi: [10.1088/2041-8205/800/2/L31](https://doi.org/10.1088/2041-8205/800/2/L31)
- Hellinger, P., Trávníček, P. M., Štverák, Š., Matteini, L., & Velli, M. 2013, *Journal of Geophysical Research (Space Physics)*, 118, 1351, doi: [10.1002/jgra.50107](https://doi.org/10.1002/jgra.50107)
- Heuer, M., & Marsch, E. 2007, *Journal of Geophysical Research (Space Physics)*, 112, A03102, doi: [10.1029/2006JA011979](https://doi.org/10.1029/2006JA011979)
- Hollweg, J. V., & Isenberg, P. A. 2002, *Journal of Geophysical Research (Space Physics)*, 107, 1147, doi: [10.1029/2001JA000270](https://doi.org/10.1029/2001JA000270)

- Hollweg, J. V., & Johnson, W. 1988, *JGR*, 93, 9547, doi: [10.1029/JA093iA09p09547](https://doi.org/10.1029/JA093iA09p09547)
- Hollweg, J. V., & Markovskii, S. A. 2002, *Journal of Geophysical Research (Space Physics)*, 107, 1080, doi: [10.1029/2001JA000205](https://doi.org/10.1029/2001JA000205)
- Horbury, T. S., Forman, M., & Oughton, S. 2008, *PRL*, 101, 175005, doi: [10.1103/PhysRevLett.101.175005](https://doi.org/10.1103/PhysRevLett.101.175005)
- Hossain, M., Gray, P. C., Pontius, Duane H., J., Matthaeus, W. H., & Oughton, S. 1995, *Physics of Fluids*, 7, 2886, doi: [10.1063/1.868665](https://doi.org/10.1063/1.868665)
- Howes, G. G., & Quataert, E. 2010, *The Astrophysical Journal Letters*, 709, L49, doi: [10.1088/2041-8205/709/1/L49](https://doi.org/10.1088/2041-8205/709/1/L49)
- Huang, S. Y., Zhang, J., Sahraoui, F., et al. 2020, *ApJL*, 897, L3, doi: [10.3847/2041-8213/ab9abb](https://doi.org/10.3847/2041-8213/ab9abb)
- Isenberg, P. A., & Lee, M. A. 1996, *JGR*, 101, 11055, doi: [10.1029/96JA00293](https://doi.org/10.1029/96JA00293)
- Jannet, G., Dudok de Wit, T., Krasnoselskikh, V., et al. 2021, *Journal of Geophysical Research (Space Physics)*, 126, e28543, doi: [10.1029/2020JA028543](https://doi.org/10.1029/2020JA028543)
- Jian, L. K., Wei, H. Y., Russell, C. T., et al. 2014, *ApJ*, 786, 123, doi: [10.1088/0004-637X/786/2/123](https://doi.org/10.1088/0004-637X/786/2/123)
- Karpman, V. I. 1974, *SSR*, 16, 361, doi: [10.1007/BF00171564](https://doi.org/10.1007/BF00171564)
- Kennel, C. F., & Engelmann, F. 1966, *Physics of Fluids*, 9, 2377, doi: [10.1063/1.1761629](https://doi.org/10.1063/1.1761629)
- Kiyani, K. H., Chapman, S. C., Khotyaintsev, Y. V., Dunlop, M. W., & Sahraoui, F. 2009, *Physical Review Letters*, 103, 075006, doi: [10.1103/PhysRevLett.103.075006](https://doi.org/10.1103/PhysRevLett.103.075006)
- Klein, K. G., Alterman, B. L., Stevens, M. L., Vech, D., & Kasper, J. C. 2018, *PRL*, 120, 205102, doi: [10.1103/PhysRevLett.120.205102](https://doi.org/10.1103/PhysRevLett.120.205102)
- Klein, K. G., Verniero, J. L., Alterman, B., et al. 2021, *ApJ*, 909, 7, doi: [10.3847/1538-4357/abd7a0](https://doi.org/10.3847/1538-4357/abd7a0)
- Leamon, R. J., Smith, C. W., Ness, N. F., Matthaeus, W. H., & Wong, H. K. 1998, *Journal of Geophysical Research*, 103, 4775, doi: [10.1029/97JA03394](https://doi.org/10.1029/97JA03394)
- Lion, S., Alexandrova, O., & Zaslavsky, A. 2016, *The Astrophysical Journal*, 824, 47, doi: [10.3847/0004-637X/824/1/47](https://doi.org/10.3847/0004-637X/824/1/47)
- Liu, W., Zhao, J., Wang, T., et al. 2023, *ApJ*, 951, 69, doi: [10.3847/1538-4357/acd53b](https://doi.org/10.3847/1538-4357/acd53b)
- Livi, R., Larson, D. E., Kasper, J. C., et al. 2022, *ApJ*, 938, 138, doi: [10.3847/1538-4357/ac93f5](https://doi.org/10.3847/1538-4357/ac93f5)
- Lotz, S., Nel, A. E., Wicks, R. T., et al. 2023, *ApJ*, 942, 93, doi: [10.3847/1538-4357/aca903](https://doi.org/10.3847/1538-4357/aca903)
- Luo, Q., Zhu, X., He, J., et al. 2022, *ApJ*, 928, 36, doi: [10.3847/1538-4357/ac52a9](https://doi.org/10.3847/1538-4357/ac52a9)
- Marsch, E. 2006, *Living Reviews in Solar Physics*, 3, 1, doi: [10.12942/lrsp-2006-1](https://doi.org/10.12942/lrsp-2006-1)
- Marsch, E., & Goldstein, H. 1983, *J. Geophys. Res.*, 88, 9933, doi: [10.1029/JA088iA12p09933](https://doi.org/10.1029/JA088iA12p09933)
- Marsch, E., Schwenn, R., Rosenbauer, H., et al. 1982, *J. Geophys. Res.*, 87, 52, doi: [10.1029/JA087iA01p00052](https://doi.org/10.1029/JA087iA01p00052)
- Marsch, E., & Tu, C. Y. 2001a, *JGR*, 106, 8357, doi: [10.1029/2000JA000414](https://doi.org/10.1029/2000JA000414)
- . 2001b, *JGR*, 106, 227, doi: [10.1029/2000JA000042](https://doi.org/10.1029/2000JA000042)
- McManus, M. D., Bowen, T. A., Mallet, A., et al. 2020, *ApJS*, 246, 67, doi: [10.3847/1538-4365/ab6dce](https://doi.org/10.3847/1538-4365/ab6dce)
- McManus, M. D., Klein, K. G., Larson, D., et al. 2023, *arXiv e-prints*, arXiv:2310.14136, doi: [10.48550/arXiv.2310.14136](https://doi.org/10.48550/arXiv.2310.14136)
- Meyrand, R., Squire, J., Schekochihin, A. A., & Dorland, W. 2021, *Journal of Plasma Physics*, 87, 535870301, doi: [10.1017/S0022377821000489](https://doi.org/10.1017/S0022377821000489)
- Ofman, L., Boardsen, S. A., Jian, L. K., Verniero, J. L., & Larson, D. 2022, *ApJ*, 926, 185, doi: [10.3847/1538-4357/ac402c](https://doi.org/10.3847/1538-4357/ac402c)
- Parker, E. N. 1958, *ApJ*, 128, 664, doi: [10.1086/146579](https://doi.org/10.1086/146579)
- Podesta, J. J., & Gary, S. P. 2011, *The Astrophysical Journal*, 734, 15, doi: [10.1088/0004-637X/734/1/15](https://doi.org/10.1088/0004-637X/734/1/15)
- Richardson, J. D., Paularena, K. I., Lazarus, A. J., & Belcher, J. W. 1995, *Geophys. Research Letters*, 22, 325, doi: [10.1029/94GL03273](https://doi.org/10.1029/94GL03273)
- Roberts, D. A., Klein, L. W., Goldstein, M. L., & Matthaeus, W. H. 1987, *JGR*, 92, 11021, doi: [10.1029/JA092iA10p11021](https://doi.org/10.1029/JA092iA10p11021)
- Sahraoui, F., Goldstein, M. L., Robert, P., & Khotyaintsev, Y. V. 2009, *Physical Review Letters*, 102, 231102, doi: [10.1103/PhysRevLett.102.231102](https://doi.org/10.1103/PhysRevLett.102.231102)
- Shankarappa, N., Klein, K. G., & Martinović, M. M. 2023, *ApJ*, 946, 85, doi: [10.3847/1538-4357/acb542](https://doi.org/10.3847/1538-4357/acb542)
- Shebalin, J. V., Matthaeus, W. H., & Montgomery, D. 1983, *Journal of Plasma Physics*, 29, 525, doi: [10.1017/S0022377800000933](https://doi.org/10.1017/S0022377800000933)
- Shklyar, D., & Matsumoto, H. 2009, *Surveys in Geophysics*, 30, 55, doi: [10.1007/s10712-009-9061-7](https://doi.org/10.1007/s10712-009-9061-7)
- Smith, C. W., Hamilton, K., Vasquez, B. J., & Leamon, R. J. 2006, *The Astrophysical Journal Letters*, 645, L85, doi: [10.1086/506151](https://doi.org/10.1086/506151)
- Smith, C. W., Stawarz, J. E., Vasquez, B. J., Forman, M. A., & MacBride, B. T. 2009, *PRL*, 103, 201101, doi: [10.1103/PhysRevLett.103.201101](https://doi.org/10.1103/PhysRevLett.103.201101)
- Smith, C. W., Vasquez, B. J., & Hollweg, J. V. 2012, *ApJ*, 745, 8, doi: [10.1088/0004-637X/745/1/8](https://doi.org/10.1088/0004-637X/745/1/8)
- Smith, W. C., Matthaeus, H. W., & Ness, F. N. 1990, in *International Cosmic Ray Conference*, Vol. 5, *International Cosmic Ray Conference*, 280

- Squire, J., Meyrand, R., Kunz, M. W., et al. 2022, *Nature Astronomy*, 6, 715, doi: [10.1038/s41550-022-01624-z](https://doi.org/10.1038/s41550-022-01624-z)
- Stix, T. H. 1992, *Waves in plasmas*
- Telloni, D., Carbone, F., Bruno, R., et al. 2019, *ApJL*, 885, L5, doi: [10.3847/2041-8213/ab4c44](https://doi.org/10.3847/2041-8213/ab4c44)
- Tu, C. Y., & Marsch, E. 1995, *Space Sci Rev*, 73, 1, doi: [10.1007/BF00748891](https://doi.org/10.1007/BF00748891)
- . 1997, *Sol Phys*, 171, 363, doi: [10.1023/A:1004968327196](https://doi.org/10.1023/A:1004968327196)
- . 2001, *JGR*, 106, 8233, doi: [10.1029/2000JA000024](https://doi.org/10.1029/2000JA000024)
- Usmanov, A. V., Goldstein, M. L., & Matthaeus, W. H. 2014, *ApJ*, 788, 43, doi: [10.1088/0004-637X/788/1/43](https://doi.org/10.1088/0004-637X/788/1/43)
- Vech, D., Mallet, A., Klein, K. G., & Kasper, J. C. 2018, *The Astrophysical Journal Letters*, 855, L27, doi: [10.3847/2041-8213/aab351](https://doi.org/10.3847/2041-8213/aab351)
- Vech, D., Kasper, J. C., Klein, K. G., et al. 2020, *ApJS*, 246, 52, doi: [10.3847/1538-4365/ab60a2](https://doi.org/10.3847/1538-4365/ab60a2)
- Verniero, J. L., Larson, D. E., Livi, R., et al. 2020, *ApJS*, 248, 5, doi: [10.3847/1538-4365/ab86af](https://doi.org/10.3847/1538-4365/ab86af)
- Verniero, J. L., Chandran, B. D. G., Larson, D. E., et al. 2022, *ApJ*, 924, 112, doi: [10.3847/1538-4357/ac36d5](https://doi.org/10.3847/1538-4357/ac36d5)
- Verscharen, D., Chen, C. H. K., & Wicks, R. T. 2017, *ApJ*, 840, 106, doi: [10.3847/1538-4357/aa6a56](https://doi.org/10.3847/1538-4357/aa6a56)
- Viñas, A. F., & Gurgiolo, C. 2009, *Journal of Geophysical Research (Space Physics)*, 114, A01105, doi: [10.1029/2008JA013633](https://doi.org/10.1029/2008JA013633)
- Walters, J., Klein, K. G., Lichko, E., et al. 2023, *ApJ*, 955, 97, doi: [10.3847/1538-4357/acf1fa](https://doi.org/10.3847/1538-4357/acf1fa)
- Wan, M., Matthaeus, W. H., Karimabadi, H., et al. 2012, *PRL*, 109, 195001, doi: [10.1103/PhysRevLett.109.195001](https://doi.org/10.1103/PhysRevLett.109.195001)
- Wicks, R. T., Alexander, R. L., Stevens, M., et al. 2016, *ApJ*, 819, 6, doi: [10.3847/0004-637X/819/1/6](https://doi.org/10.3847/0004-637X/819/1/6)
- Woodham, L. D., Wicks, R. T., Verscharen, D., & Owen, C. J. 2018, *The Astrophysical Journal*, 856, 49, doi: [10.3847/1538-4357/aab03d](https://doi.org/10.3847/1538-4357/aab03d)
- Woodham, L. D., Wicks, R. T., Verscharen, D., et al. 2019, *ApJL*, 884, L53, doi: [10.3847/2041-8213/ab4adc](https://doi.org/10.3847/2041-8213/ab4adc)
- Wu, H., Tu, C., He, J., Wang, X., & Yang, L. 2022, *ApJ*, 926, 116, doi: [10.3847/1538-4357/ac4413](https://doi.org/10.3847/1538-4357/ac4413)
- Wüest, M., Evans, D. S., & von Steiger, R. 2007, *Calibration of Particle Instruments in Space Physics*
- Zhao, G. Q., Lin, Y., Wang, X. Y., et al. 2021, *ApJ*, 906, 123, doi: [10.3847/1538-4357/abca3b](https://doi.org/10.3847/1538-4357/abca3b)

APPENDIX

A. NUMERICAL DETERMINATION OF QUASILINEAR HEATING RATE

Determination of Q_{ICW} and $Q(v_{\perp}, v_{\parallel})$ is obtained through integrating Eq 12 by parts to obtain

$$Q_{\text{ICW}} = -\pi^2 \Omega_p^2 m_p \int_{-\infty}^{\infty} dv_{\parallel} \int_0^{\infty} dv_{\perp} \left[\int_0^{\infty} dk_{\parallel} v_{\perp}^2 \delta(\omega_k - k_{\parallel} v_{\parallel} - \Omega_p) \frac{\omega_k^2}{k_{\parallel}^2} I(k_{\parallel}) \hat{G}_k \bar{g}(v_{\perp}, v_{\parallel}) \right] \quad (\text{A1})$$

The δ -function in Eq 12& A1 corresponds to the ICW resonance condition, and defines a single parallel wave number that resonates with particles at each parallel velocity. Change of variables yields a δ -function for resonant wave number $k_{res}(v_{\parallel})$ as

$$\delta(\omega_k - k_{\parallel} v_{\parallel} - \Omega_p) = \frac{\delta(k_{\parallel} - k_{res})}{|v_g(k_{res}) - v_{\parallel}|}, \quad (\text{A2})$$

where $v_g(k_{res}) = \partial\omega_k/\partial k|_{k_{res}}$ is the group speed evaluated at each k_{res} . For positive k_{\parallel} , taken as outward going ICWs, there is no resonance unless $v_{\parallel} < 0$, limiting our concern only to negative thermal speeds. We use the δ -function to substitute $k_{res}(v_{\parallel})$ for k_{\parallel} , thereby evaluating the integral over wavenumber, Eq A1 becomes

$$Q_{\text{ICW}} = -\pi^2 \Omega_p^2 m_p \int_{-\infty}^0 dv_{\parallel} \int_0^{\infty} dv_{\perp} \left[\frac{v_{\perp}^2}{|v_g(k_{res}) - v_{\parallel}|} \frac{\omega_{k_{res}}^2}{k_{res}^2} I(k_{res}) \hat{G}_k \bar{g}(v_{\perp}, v_{\parallel}) \right], \quad (\text{A3})$$

where the spectrum $I(k_{\parallel})$ is interpolated from k_{\parallel} to k_{res} , constructing $I(k_{res})$. Eq A3 is entirely a function of v_{\parallel} and v_{\perp} and can be calculated via a numerical integration over velocity space. We further identify the differential heating rate

$$Q(v_{\perp}, v_{\parallel}) = -\pi^2 \Omega_p^2 m_p \frac{v_{\perp}^2}{|v_g(k_{res}) - v_{\parallel}|} \frac{\omega_{k_{res}}^2}{k_{res}^2} I(k_{res}) \hat{G}_k \bar{g}(v_{\perp}, v_{\parallel}). \quad (\text{A4})$$

To perform the numerical integral in Eq A3, we evaluate $Q(v_{\perp}, v_{\parallel})$ on a 1 km/s \times 1 km/s grid, which was found to be sufficient for convergence of Eq A3. The range of integration is set to -1000 km/s $< v_{\parallel} < 0$ km/s and 0 km/s $< v_{\perp} < 1000$ km/s. We have removed contributions to the spectra with $k_{\parallel} d_i < 0.3$ and $k_{\parallel} d_i > 5$, which for $\beta_p = 0.1$ corresponds to an approximate range of thermal speeds between 0.02 and 7.5 $v_{th\parallel}$. Figure 5(a&b) shows that the parallel thermal speeds hovers near 50 km/s over this entire interval. Thus, the 1000km/s limits are sufficiently large with respect to the thermal and Alfvén speeds for this stream that there are no significant contributions in portion of phase space out of the bounds of integration. The heating rate as a function of parallel resonant velocity $Q(v_{\parallel})$ is computed by integrating $Q(v_{\perp}, v_{\parallel})$ over perpendicular velocities.

These methods have previously been used to obtain heating rates Q_{ICW} of order $\sim 10\%$ of the turbulent cascade rate (Bowen et al. 2022) though this previously studied interval contained significantly less amounts of left-hand polarized waves than this stream. Our results shown in Fig 5 suggest that a great amount of the turbulent energy likely enters the plasma via cyclotron resonant heating.

B. APPLICATION OF NON-PARAMETRIC REPRESENTATIONS

While in situ observations of the proton velocity distribution have long been recognized to have a mostly Gaussian shape (Marsch & Goldstein 1983) and drifting biMaxwellian approximation has regularly been used to approximate ion velocity distributions (Marsch et al. 1982; Marsch & Tu 2001b; Tu & Marsch 2001; Heuer & Marsch 2007; Klein et al. 2021; Verniero et al. 2022; McManus et al. 2023); however, it is clear that deviations from nonthermal structure in the velocity distribution can affect wave-particle resonant processes (Dum et al. 1980; Bowen et al. 2022; Walters et al. 2023). Furthermore, it is well known that the equilibrium kinetic contours for dispersive ICW resonance do not coincide with Maxwellian curvature (Isenberg & Lee 1996), such that relaxation via ICW resonant processing cannot be entirely captured via bi-Maxwellian approximations (Heuer & Marsch 2007). In this sense it is important to test the heating rates computed from the drifting biMaxwellian model in Equation 11 against heating rates computed from non-parametric models of the velocity distribution.

B.1. Hermite Polynomial Interpolation

Bowen et al. (2022) previously used linear least-square fits of orthogonal Hermite-polynomials to estimate non-Maxwellian features in the velocity distribution; following this previously developed method, we perform a linear least square fit to the average proton velocity distribution in each 128s interval using the Hermite polynomials H_n , and Hermite functions ϕ_m

$$\bar{g}^H(v_\perp, v_\parallel) = \sum_{m,n} A_{mn} \phi^m(v_\perp/w_{\perp th}) \phi^n(v_\parallel/w_{\parallel th}) \quad (\text{B5})$$

$$H_n(v) = (-1)^n e^{v^2} \frac{d^n}{dx^n} e^{-v^2} \quad (\text{B6})$$

$$\phi^m = \frac{H^m(v)}{\sqrt{2^m \pi^{1/2} m!}} e^{-v^2}. \quad (\text{B7})$$

We fit an orthogonal set of Hermite functions to each velocity distribution through constructing the matrix \mathbf{A} , which consists of the transform coefficients A_{mn} corresponding to each two-dimensional Hermite polynomial combination. Through linear least square fitting of Φ , with elements $\phi^m \phi^n$, to the observed velocity distribution, written as matrix \mathbf{g} such that $\mathbf{g} = \mathbf{A}\Phi$ and least square fit inversion gives:

$$\mathbf{A} = \mathbf{g}\Phi^T (\Phi\Phi^T)^{-1}, \quad (\text{B8})$$

where a singular value decomposition determines the pseudo-inverse of $\Phi\Phi^T$. The matrix \mathbf{A} then gives the best-fit coefficients for the Hermite polynomial composition.

We furthermore adopt errors on \mathbf{g} associated with Poisson counting, such that the uncertainty at each velocity coordinate k is $\sigma_{g_k} = \sqrt{g_k}$ (Wüest et al. 2007). Poisson noise between energy bins is uncorrelated such that we construct the diagonal-weight matrix as \mathbf{W} with entries σ^2 can be included in weighted linear least square fitting as $\mathbf{g}\mathbf{W} = \mathbf{A}\Phi\mathbf{W}$ such that

$$\mathbf{A} = \mathbf{g}\mathbf{W}\Phi^T (\Phi\mathbf{W}\Phi^T)^{-1} \quad (\text{B9})$$

The coefficients \mathbf{A} are then used to construct $\bar{g}^H(v_\perp, v_\parallel)$ using Equation B5.

Using $\bar{g}^H(v_\perp, v_\parallel)$, which is an analytic, differentiable function, it is possible to separately estimate Q_{ICW} without the assumption of a drifting bi-Maxwellian structure to the velocity distribution.

B.2. Radial Basis Function Interpolation

We further include another approximation to the velocity distributions through interpolation via radial basis functions (RBFs) (Broomhead & Lowe 1988; Bowen et al. 2023) to model the distribution function via a summed set of interpolating functions given by

$$g_p^{RBF}(v_\perp, v_\parallel) = \sum_i^{N_{RBF}-1} R_i \psi_i(\zeta_i), \quad (\text{B10})$$

with $\zeta_i = \mathbf{v} - \mathbf{v}_i^c$, where \mathbf{v}_i^c is the center of each interpolating RBF, denoted by ψ_i . The RBF method requires choice of a basis function, ψ , which we choose to be an isotropic 2D bi-Maxwellian

$$\psi_i(v_\perp, v_\parallel) = \frac{1}{\sqrt{\pi^3} w_{RBFi}^3} \exp \left[-\frac{(v_\perp - v_{\perp i}^c)^2}{w_{RBFi}^2} - \frac{(v_\parallel - v_{\parallel i}^c)^2}{w_{RBFi}^2} \right]. \quad (\text{B11})$$

The number of interpolating functions, N_{RBF} , must be specified along with the thermal speed w_{RBFi} and central location, \mathbf{v}_i^c , of each of the ψ_i implemented in the interpolation. In principle, w_{RBFi} does not need to be isotropic and can vary for each ψ_i ; however, we determine that setting a Maxwellian-RBF at each measured SPAN energy bin with nonzero phase space density gives suitable results. Furthermore, we uniformly set $w_{RBF} = 40$ km/s, which we find is suitable for interpolating the proton distribution.

The interpolated velocity distribution via radial basis functions is then given by

$$\bar{g}^{RBF}(v_\perp, v_\parallel) = \sum_i^{N_{RBF}-1} R_i \psi_i(\zeta), \quad (\text{B12})$$

with $\zeta = \vec{v} - \vec{v}_c$. Determination of the weights R_i is again performed through SVD estimation for the pseudoinverse giving a least square fit of \bar{g}^{RBF} to the observed velocity distribution. We again compute the RBF on each 128s average velocity distribution and include weighted errors in the least square fit corresponding to Poisson noise analogous to Eq B9.

B.3. Comparing Model Distributions

To verify the heating of the plasma via ICW resonant interactions, we recompute Equation 12 using the Hermite polynomial and radial basis function approximations to the proton distribution, $\bar{g}^H(v_\perp, v_\parallel)$ and $\bar{g}^{RBF}(v_\perp, v_\parallel)$, we refer to the heating rates computed from Equation 12 via the drifting biMaxwellian, Hermite polynomials, and RBF interpolation as Q_{BM} , Q_{HMTE} , and Q_{RBF} respectively, we also compute the average heating rate of the three terms Q_{AVG} . Note that the ICW spectrum $I(k_\parallel)$ is unaffected by the choice of model as $d_i = V_A/\omega_c$ is a function only of the magnetic field strength and total plasma density, which are independent of the kinetic phase-space distribution.

The top row of Figure 6, panels (a-c), respectively show Q_{HMTE} , Q_{RBF} , and Q_{AVG} against Q_{BM} . While all computed heating rates have the same qualitative behavior, i.e. positive valued indicating the absorption of ICWs and plasma heating via cyclotron resonance, Q_{HMTE} tends to systematically underestimate the heating rates predicted by Q_{BM} , whereas Q_{RBF} tends to overestimate Q_{BM} . The average of all heating rates Q_{AVG} closely follows Q_{BM} , thus Q_{BM} was chosen as the value reported in the body of the manuscript.

The bottom panels shows statistics on the quality of the various models. To compare the quality of the relative models we compute two parameters. Figure 6(d) shows the distribution of measured Pearson correlation coefficients between the logarithm of the observed distribution $\text{Log}_{10}g_p(v_\perp, v_\parallel)$ and the three models $\text{Log}_{10}\bar{g}^{BM}(v_\perp, v_\parallel)$, $\text{Log}_{10}\bar{g}^H(v_\perp, v_\parallel)$, and $\text{Log}_{10}\bar{g}^{RBF}(v_\perp, v_\parallel)$. High levels of correlation indicate that the model correctly matches the observed distribution. The use of the logarithm of the distribution in computing the Pearson R^2 correlation coefficient allows for weighting of the entirety of phase space and includes the regions where ICW resonant interactions are most important; without the logarithmic weighting, the correlation coefficient is mostly dominated by the models performance at the peak of the distribution. We find R^2 is largest for the RBF interpolation and smallest for the parametric drifting biMaxwellian fit. Interestingly, the level of heating computed between these models remains relatively constant even though the R^2 values vary, this suggests that variations between the three models are mostly occurring in regions that are not resonant with the outward going ICWs. We speculate these differences are likely due to the models ability to approximate the ion-beam population.

We also compute the χ^2 of each of the models. Given the nature of the nonlinear fitting there is lack of clear number of degrees of freedom. Furthermore errors in the model are not likely to obey Gaussian statistics. For these reasons hypothesis testing via the χ^2 statistic is not possible. To determine the quality of the fits we compare the ratio of χ^2 to the value compared for the biMaxwellian, χ_{BM}^2 . Figure 6(e) shows the distribution of the logarithmic ratio of χ_{RBF}^2/χ_{BM}^2 and $\chi_{HMTE}^2/\chi_{BM}^2$. The RBF model tends to perform much netter than the drifting biMaxwellian with a uniform $\chi_{RBF}^2/\chi_{BM}^2 < 1$. In terms of χ^2 , the Hermite polynomial approximation tends to have a similar performance to the drifting biMaxwellian fit in this stream, though the Pearson correlation is significantly better than the biMaxwellian fit. Again, the ability of each of models to reproduce similar heating rates, but with significantly different χ^2 suggests that the main difference in the models may be in reproducing the ion-beam. Our future work will investigate further the role of the ion-beam in these processes.

In any case, the use of these various parametric and non-parametric models for the observed proton distribution function all recover heating rates that suggest that ICW are absorbed into the core of the proton distribution, resulting in plasma heating via ICW resonance. These results suggest that the model used may not be inherently important in understanding ICW heating of the proton core.

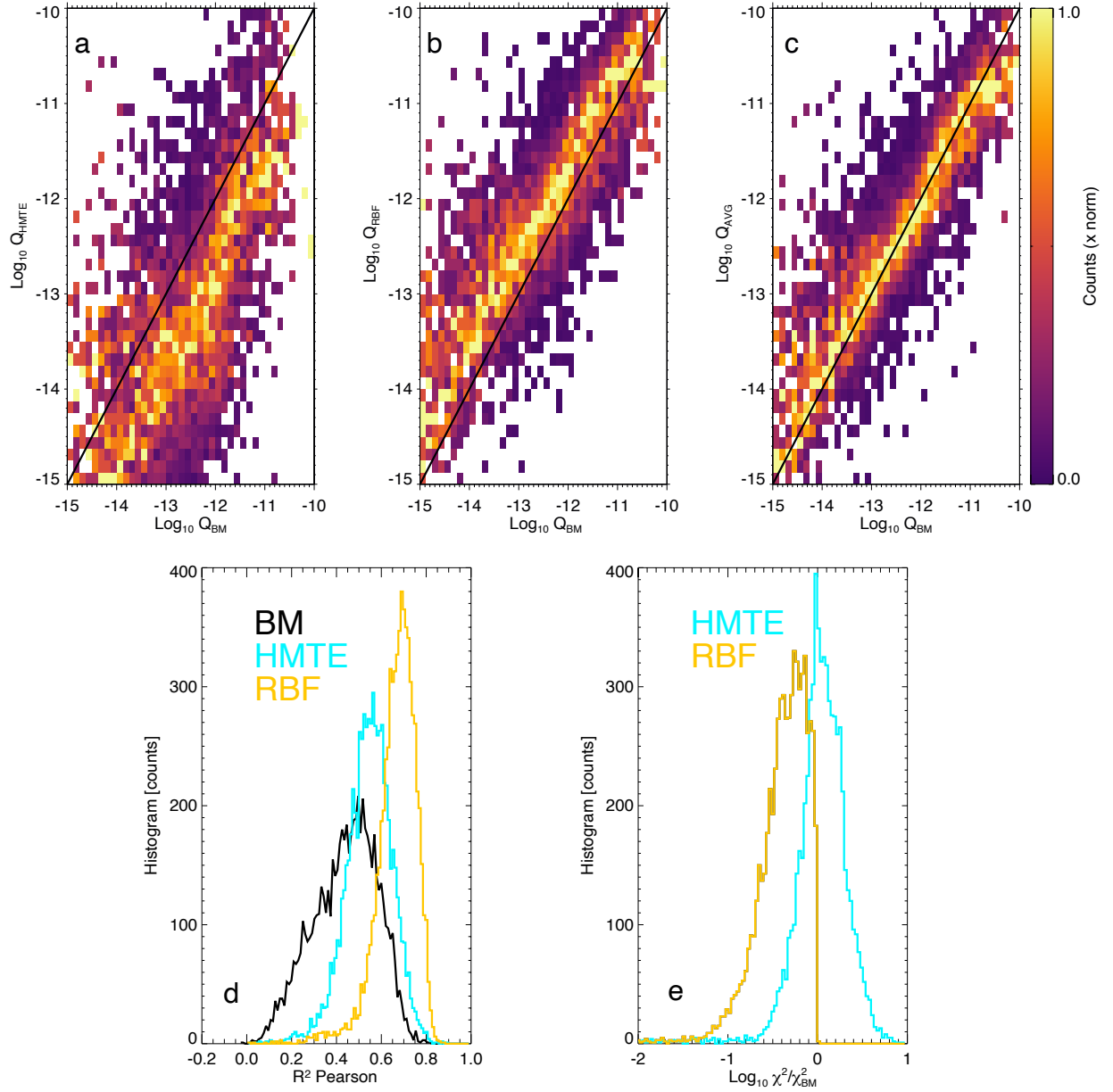


Figure 6. a) 2D histogram of Q_{HMTE} against Q_{BM} for each of the 6737 studied intervals; data are column normalized and the black line shows $Q_{HMTE} = Q_{BM}$. b) Same as panel a, but with Q_{RBF} against Q_{BM} . c) Same as panel a, but with the average of all three heating rates Q_{AVG} against Q_{BM} . d) Histogram showing distributions of Pearson R^2 correlation between the 6737 modeled distributions and observed SPANi distributions; drifting biMaxwellian (BM) in black; Hermite (HMTE) in teal; radial basis function (RBF) in orange. e) Histogram showing distributions of χ_{RBF}^2/χ_{BM}^2 (orange) and $\chi_{HMTE}^2/\chi_{BM}^2$ (teal) on a logarithmic scale.